Available online at www.sciencedirect.com
ScienceDirect
Journal of the European Ceramic Society 31 (2011) 1439–1449
www.elsevier.com/locate/jeurceramsoc

Characterisation of plasma-sprayed $SrFe_{12}O_{19}$ coatings for electromagnetic wave absorption

K. Bobzin [a], G. Bolelli [b,*], M. Bruehl [a], A. Hujanen [c], P. Lintunen [c], D. Lisjak [d], S. Gyergyek [d], L. Lusvarghi [a]

[a] *Surface Engineering Institute, RWTH Aachen University, Kackertstrasse 15, 52072 Aachen, Germany*
[b] *Department of Materials and Environmental Engineering, University of Modena and Reggio Emilia, Via Vignolese 905, 41125 Modena, Italy*
[c] *VTT Technical Research Centre of Finland, P.O. Box 1000, FIN-02044 VTT, Finland*
[d] *Jožef Stefan Institute, Department for Materials Synthesis, Jamova 39, 1000 Ljubljana, Slovenia*

Received 17 September 2010; received in revised form 17 January 2011; accepted 3 February 2011
Available online 2 March 2011

Abstract

$SrFe_{12}O_{19}$ coatings, intended as electromagnetic wave absorbers, were produced by atmospheric plasma spraying (APS) using two different kinds of feedstock powders: spray-dried agglomerates of micrometric $SrFe_{12}O_{19}$ particles (type-A) or spray-dried agglomerates of raw materials ($SrCO_3$, Fe_2O_3), reactively sintered at 1100 °C (type-B).

During spraying, type-A agglomerates either remain unmelted, producing porous coating regions where crystalline hexaferrite is retained, or are disrupted into smaller granules which melt completely, resulting in dense coating regions with no crystalline hexaferrite.

The sintered type-B agglomerates possess higher cohesive strength and do not fall apart: the finer ones melt completely, whereas, in the larger ones, the outer region melts and infiltrates the porous unmelted core which retains crystalline hexaferrite. Dense coatings can therefore be obtained while preserving high amounts of crystalline hexaferrite even inside the dense areas. Such coatings show magnetic properties that are promising for electromagnetic wave absorption applications.

Keywords: Ferrites; Atmospheric plasma spraying; Magnetic properties; Functional applications; Hard magnets

1. Introduction

The demand for absorbers of electromagnetic waves has recently increased, because of the need to suppress electromagnetic noise and to prevent electromagnetic interference phenomena, caused by an extensive exploitation of electromagnetic waves in modern technology (electronics, wireless communication, telecommunications...).[1–4] Suitable materials for the production of microwave and mm-wave absorbers are hexaferrites. These are ferrimagnetic Fe-containing oxides based on the $MFe_{12}O_{19}$ (M = Ba, Sr, etc.) compound, which has a complex magnetoplumbite structure[5] where Fe ions occupy five different interstitial positions between closely packed M^{2+} and O^{2-} ions. The anisotropic structure and the specific site occupancy of the Fe ions produce very high magnetocrystalline anisotropy. These materials behave as ferrimagnets and possess considerable magnetic permeability (μ) also at high frequencies (up to 50 GHz). The magnetic losses (described by the imaginary part of the magnetic permeability μ'') attain a maximum at the ferromagnetic resonance (FMR) frequency where a strong absorption of electromagnetic waves occurs. This makes the basic $MFe_{12}O_{19}$ suitable for mm-wave applications; for microwave absorption, the frequency of ferromagnetic resonance has to be reduced by decreasing the magnetocrystalline anisotropy through a partial substitution of Fe ions with $Me^{II}M^{IV}$, where Me = Mn, Co, Ni, Zn and M = Ti, Sn, Ir, Rh.[6–11]

Pure hexaferrite-based ceramics are commercially available as sintered tiles or plates; therefore, there are obvious limitations in the possibility to adjust them to the wide variety of shapes of real components requiring electromagnetic protection. Higher flexibility could be attained by applying hexaferrite layers directly onto such components using thermal spraying

* Corresponding author. Tel.: +39 059 2056233; fax: +39 059 2056243.
E-mail address: giovanni.bolelli@unimore.it (G. Bolelli).

0955-2219/$ – see front matter © 2011 Elsevier Ltd. All rights reserved.
doi:10.1016/j.jeurceramsoc.2011.02.003

processes. Despite the wide industrial diffusion of thermal spraying for the preparation of a large variety of coatings,[12,13] their use for the deposition of electromagnetically active layers has, up to now, been scarce. Among the few examples, Bartuli et al.[14] prepared absorbing coatings based on lossy conductors, dielectrics and spinel ferrites by thermal spraying. Other studies considered the preparation of spinel ferrite coatings,[15–18] but the crystalline structure of the material was altered by the spraying process, so that annealing was necessary for the crystallisation of ferrite phases. The crystallisation of $BaFe_{12}O_{19}$ coatings prepared from Ba- and Fe-nitrate solutions by inductively coupled plasma technique was achieved only when the substrates were kept at 600–900 °C.[19]

Since the use of high deposition temperatures and/or of post-process heat treatments limits the applicability of thermally sprayed ferrite layers, a further research has been undertaken in order to verify the possibility to use thermal spraying for the direct deposition of hexaferrite layers with suitable phase composition and magnetic properties.

The results obtained so far were mainly focused on Ba-hexaferrites. They have shown that, when processing $BaFe_{12}O_{19}$ and $BaCoTiFe_{10}O_{19}$ compounds by atmospheric plasma spraying (APS) or HVOF-spraying, excessively "hot" process parameters result in the formation of undesirable secondary phases[20,21]; therefore, the retention of large amounts of crystalline hexaferrite requires special adjustments.

On the one hand, the spray parameters and the size distribution of the feedstock powder have to be optimised in order to embed a controlled fraction of unmelted material in the sprayed layer while retaining sufficient deposition efficiency[22,23]; specifically, the best results were obtained using the APS technique.[22]

On the other hand, the production route of the feedstock powder also plays a crucial role. APS-processing of spray-dried agglomerates of fine Ba-hexaferrite particles gave rise to coatings with "bimodal" microstructure, where dense regions, produced by molten agglomerates and containing no crystalline hexaferrite, surround unmelted regions containing the original micron-sized hexaferrite particles.[22] On the contrary, reactively sintered hexaferrite agglomerates gave different results. Reactively sintered agglomerates were produced by spray-drying a stoichiometric mixture of micrometric reagent particles ($BaCO_3 + Fe_2O_3$ in the case of Ba-hexaferrite) and by heat-treating the resulting agglomerates in order to promote reaction and develop crystalline hexaferrite. The resulting APS coatings contained crystalline hexaferrite both in the porous unmelted regions and in the dense ones.[23]

The aim of the present research is therefore to study the deposition of $SrFe_{12}O_{19}$ (Sr-hexaferrite) coatings by APS using both spray-dried agglomerates of micrometric Sr-hexaferrite particles and reactively sintered agglomerates. Particularly, the paper focuses on the different microstructures and phase distributions within the coatings obtained by using these two kinds of feedstock, investigated by SEM, XRD and micro-Raman spectroscopy. Moreover, the magnetic properties of the coatings were also examined and electromagnetic absorption was estimated.

2. Materials and methods

2.1. Powder production

Two different kinds of feedstock powders suitable for thermal spray use, both having $SrFe_{12}O_{19}$ composition, were produced.

The first kind of feedstock powder (type-A) consisted of spray-dried spherical agglomerates of micrometric $SrFe_{12}O_{19}$ particles. These latter were synthesized by solid-state reaction from $SrCO_3$ (Merck, Darmstadt, Germany, 98.5% pure) and Fe_2O_3 (NK-α SEW, IROX-NKK Co. Ltd., Tokyo, Japan, 99.65% pure) in 1–2 kg batches. The reagents were homogenized in stoichiometric amounts in a water/ethanol slurry for 1 h using a Turbula homogenizer (System Schatz Type T2F, Willy A. Bachofen AG, Maschinenfabrik, Basel, Switzerland). After drying at 80 °C, the powders were calcined at 1100 °C for 3 h and then attrition-milled for 2 h at 200 rpm speed. The resulting particles, whose size was of 1–2 μm, were agglomerated into spherical granules, using a spray-drier attached to a cyclone (Niro pilot P6.3, GEA Niro Inc., Columbia, USA): the coarser agglomerates, with sizes approximately >20 μm (Fig. 1A), suitable for APS, were collected at the bottom of the spray-drying chamber and were separated from the finer ones collected into the cyclone.

Using the calcined and attrition-milled micrometric particles, a bulk sample was also produced in order to assess the intrinsic permeability and permittivity of the $SrFe_{12}O_{19}$ compound (see Section 2.3). For this purpose, the particles were uniaxially pressed and sintered at 1300 °C for 1 h.

The second kind of feedstock powder (type-B) consisted of reactively sintered agglomerates of reagent particles. This powder was therefore based on a stoichiometric blend of the above-mentioned $SrCO_3$ and Fe_2O_3 reagents. These reagent particles were first homogenized in a water/ethanol slurry for 1 h using the Turbula homogenizer; then, this powder mixture was dispersed in water with the aid of a dispersing agent and was spray-dried to achieve spherical agglomerations (Niro pilot P6.3) and the finer agglomerates (approximately <20 μm), unsuitable for APS processing, were separated through the cyclone as mentioned previously. The spherical agglomerates were then heat-treated at 1150 °C for 4 h to achieve reactive sintering, so that all of the original reagents were converted to Sr-hexaferrite phase. Since part of the agglomerates collapsed during this treatment, the sintered feedstock was classified using a 20 μm sieve to separate the finer particles.

2.2. Coating deposition

Type-A (spray-dried hexaferrite particles) and type-B (reactively sintered agglomerates) powders were processed by the APS system F4-HBS from Sulzer Metco (Hattersheim, Germany). All of the coatings were deposited onto a glass–ceramic substrate, grit-blasted before spraying. The glass–ceramic substrate was chosen because of its non-magnetic characteristics, which make it suitable for the measurement of the magnetic properties of the coatings. Based on some preliminary testing, it was decided that slightly different process

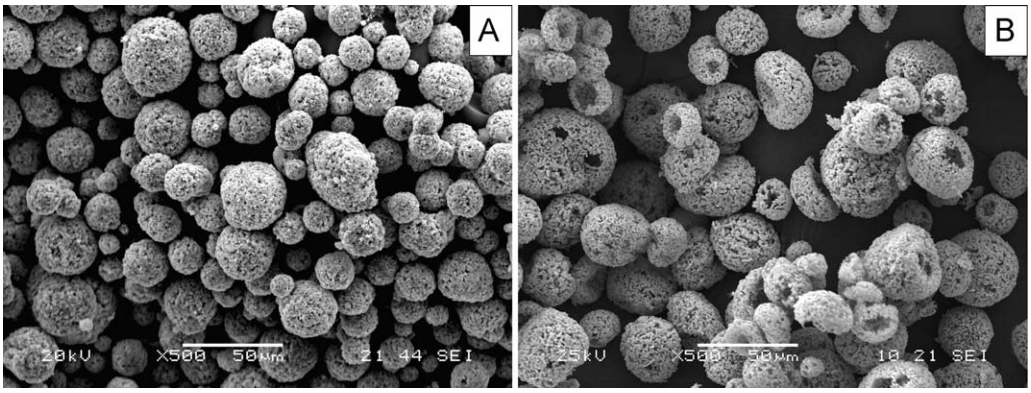

Fig. 1. SEM micrographs (secondary electrons) of type-A (A) and type-B (B) feedstock powders.

parameters (including different spray distance values) had to be employed with the two kinds of feedstock powder in order to achieve acceptable deposition efficiencies and substrate adhesion; therefore, it was not possible to adopt identical parameter sets in the two cases. Three different coatings were produced with each kind of powder, the selected parameters are summarised in Table 1.

2.3. Characterisation of powders and coatings

The particle size distribution of both feedstock powders was measured with a Lecotract-LT100 (St. Joseph, Michigan, USA) particle size analyzer. X-ray diffraction (XRD) was employed in order to assess the phase composition of the powders and coatings. Specifically, an X'Pert PRO diffractometer (PANAlytical, Almelo, The Netherlands) with Cu-Kα radiation was used for type-A feedstock and for the coatings, whereas a PW 1830 diffractometer (Philips, The Netherlands) with Mo-Kα radiation was employed for type-B feedstock. The morphology of the powders was observed by scanning electron microscopy (SEM: JSM-6360LV, JEOL, USA). Cross-sectional samples of the coatings, prepared by metallographic cutting, cold-mounting in polyester resin, grinding with SiC papers (up to 2500 mesh) and polishing with diamond slurry (up to 0.5 μm), were also observed by SEM (XL30 and Quanta 200, FEI, Eindhoven, The Netherlands), and additional SEM micrographs were acquired on fractured sections of the coatings. The polished cross-sections were also studied by micro-Raman spectroscopy (LabRAM, Horiba Jobin-Yvon, Longjumeau, France; laser wavelength: 632.81 nm).

The magnetic properties of the coatings under a static magnetic field were measured with the vibrating sample magnetometer (VSM: model 7312, Lake Shore, Westerville, OH, USA) under a maximum applied field of 1.35 T; for this purpose, parts of the coatings were detached from the substrate and powdered.

Additionally, in order to ascertain the actual usefulness of basic $SrFe_{12}O_{19}$ compound for mm-wave applications, the permeability and permittivity of a bulk $SrFe_{12}O_{19}$ sample (prepared as specified in Section 2.1) were computed from the S-parameters determined with a Vector Network Analyzer (model 8510C, Agilent, Santa Clara, CA, USA) by using transmission line analogy. The rectangular $SrFe_{12}O_{19}$ sample was placed inside standard WR19 waveguide (1.88 mm × 3.759 mm). The measurement method is basically the same as described in the 8510 product note.[24]

3. Results and discussion

3.1. Characterization of the feedstock powders

Both kinds of feedstock powders (type-A and type-B) consist of pure crystalline hexaferrite (Fig. 2) and, since they were both subjected to a spray-drying process, they both exhibit the typical spherical morphology (Fig. 1). In the type-B feedstock, the sintering process was accompanied by a solid-state reaction between the original reagent particles, which were completely exhausted; moreover, this process did not alter the original morphology imparted by spray-drying, apart from a minor fraction of collapsed fine particles which were eliminated by sieving (Section 2.1). This is important in order to ensure the powder has adequate flowability for the APS process. The particle size

Table 1
APS process parameters.

Sample label	Feedstock type	Primary gas (Ar) flow rate (Slpm)	Secondary gas (H_2) flow rate (Slpm)	Carrier gas flow rate (Slpm)	Stand-off distance (mm)	Powder injection angle (°)
SrM-1	Type-A	50	6	3.5	100	90
SrM-2	Type-A	50	0	3.5	100	90
SrM-3	Type-A	50	0	3.5	100	105
OM-1	Type-B	50	6	3.5	130	90
OM-2	Type-B	50	0	3.5	130	90
OM-3	Type-B	60	0	3.5	130	90

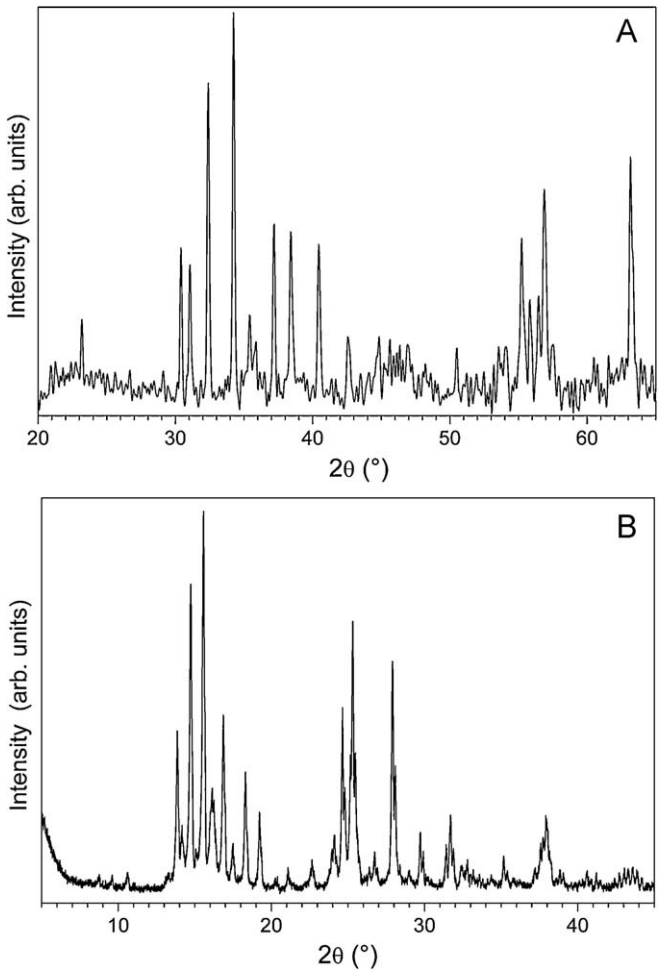

Fig. 2. XRD patterns of type-A (A) and type-B (B) feedstock powders, acquired using Cu-Kα and Mo-Kα radiations, respectively.

analysis by laser diffraction indicates that type-A feedstock possesses $d_{10} = 18\ \mu m$, $d_{50} = 29\ \mu m$, $d_{90} = 48\ \mu m$, whereas type-B feedstock exhibits $d_{10} = 22\ \mu m$, $d_{50} = 37\ \mu m$, $d_{90} = 60\ \mu m$.

3.2. Structural and microstructural characterisation of APS coatings

Irrespective of the type of feedstock, the use of H_2 in the plasma jet resulted in very dense layers, with no unmelted material; indeed, the higher enthalpy and higher thermal conductivity which H_2 confers to the plasma jet caused complete melting of the original agglomerates (Figs. 3A and 4A). Even individual lamellae are hardly discernible in the SrM-1 and OM-1 coatings: the heat delivered from the impinging molten droplets and from the plasma jet to the previously deposited layers was sufficient to trigger some interlamellar welding processes, so that the microstructure resembles the one obtained with materials having low melting or softening temperature (e.g. oxide glasses[25,26]), where such interlamellar sintering is more likely. Very large quenching stresses arising in those stackings of well-bonded lamellae[27,28] also cause extensive transverse microcracking across the coating.

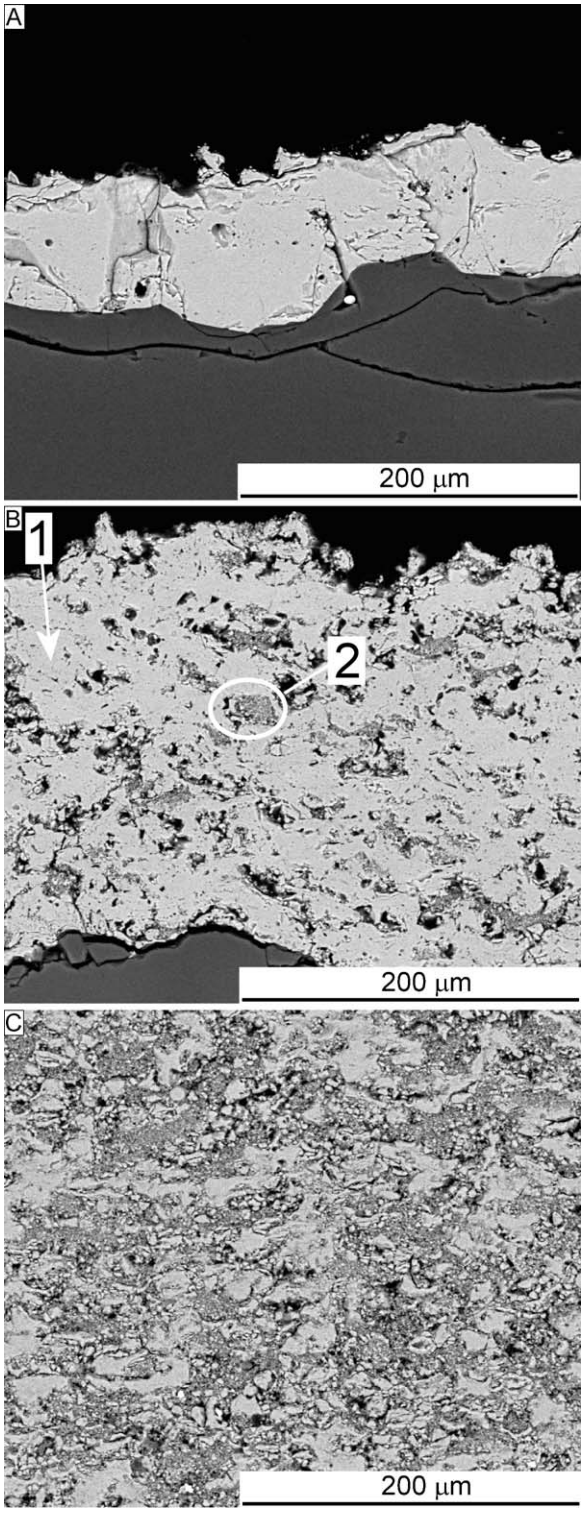

Fig. 3. Cross-sectional SEM micrographs of the SrM-1 (A), SrM-2 (B) and SrM-3 (C) coatings, obtained using type-A feedstock. Labels: 1 = dense region and 2 = porous region.

Previous studies on plasma- and HVOF-sprayed Ba-hexaferrites clearly showed that, when such extensive melting of the sprayed agglomerates occurred, no hexaferrite phase could ever be retained in the coatings,[20–22] because the time required to complete the crystallisation process of Ba-hexaferrite, which

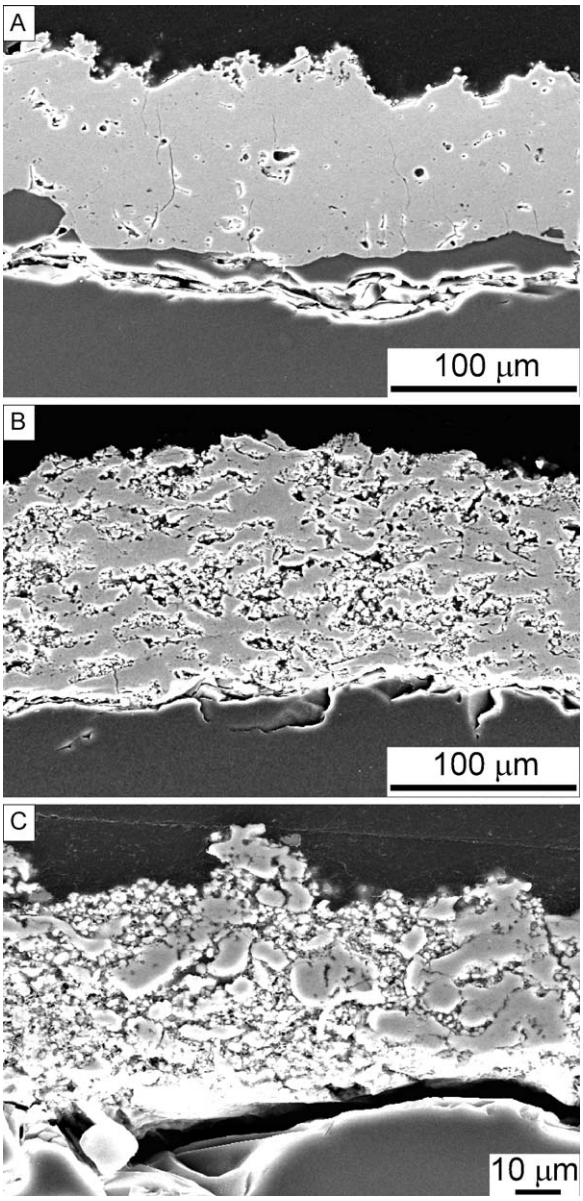

Fig. 4. SEM micrographs of the OM-1 (A), OM-2 (B) and OM-3 (C) coatings, obtained using type-B feedstock.

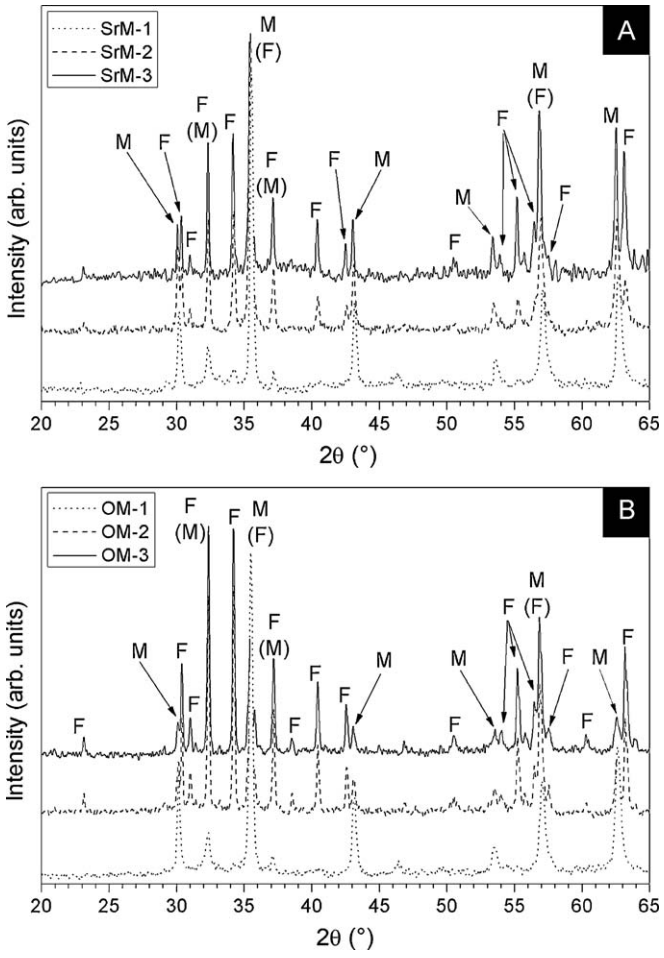

Fig. 5. XRD patterns of the coatings deposited using type-A (A) and type-B (B) feedstock. Legend: M = magnetite (JC-PDS card 19-629), F = $SrFe_{12}O_{19}$ hexagonal ferrite (JC-PDS card 33-1340).

involves various peritectic reactions,[29] is definitely too long, compared to the very short solidification times (of the order of few microseconds, with cooling rates of $\sim 10^6$ K/s) of impact-quenched molten lamellae.[30,31] A similar phenomenon can be expected for Sr-hexaferrite as well; indeed, according to the most recent phase diagram published on the $SrO–Fe_2O_3$ system,[32] the Sr-hexaferrite compound exhibits incongruent melting: as temperature increases, the stoichiometric hexagonal ferrite compound is progressively altered by three peritectic reactions, each involving loss of oxygen and partial reduction of some Fe^{3+} to Fe^{2+}. After the last peritectic reaction, magnetite is formed in equilibrium with a Sr-rich liquid phase. During solidification, magnetite is therefore the first phase developed from the liquid.[32] Accordingly, the XRD patterns of the SrM-1 and OM-1 coatings exhibit only a few very weak peaks of crystalline Sr-hexaferrite (Fig. 5A and B), whereas nearly all of the diffraction peaks can be indexed to a spinel structure (such as magnetite, JC-PDS file 19-629): obviously, because of the high cooling rate during impact quenching, the solidification process was arrested before the first peritectic reaction could take place, so that magnetite was retained. A weak, broad diffraction band also emerges at $30° < 2\theta < 40°$: it reflects the formation of a poorly crystalline secondary phase from the quenched residual melt. Hypotheses can be made on the nature of this secondary phase. The broad band is compatible with a glassy structure; accordingly, amorphous phases have often been observed in impact-quenched lamellae[33] and in thermally sprayed coatings, especially when complex oxides are employed.[34,35] For instance, in thermally sprayed $BaTiO_3$, a band located at $23° < 2\theta < 33°$ was reported,[34,35] which is consistent with that of amorphous perovskites.[36] A weak diffraction band located between 30° and 40°, similar to the one observed in the present patterns, was accordingly reported for amorphous Ba hexaferrite[37] and similar bands, centred at 2θ angles slightly larger than 30°, were also found in other iron-based amorphous oxides.[38,39] This could support the hypothesis of a Sr-rich iron-based glassy phase as a result of the rapid cooling of the residual melt in the present coatings.

Alternatively, very small and highly defective perovskite-type crystals, with chemical formula close to $SrFeO_3$, could have been developed. The main X-ray diffraction peak of Sr,Fe-containing perovskites is indeed located at $2\theta = 32–33°$,[40,41] so that a poorly crystalline structure of that kind would be compatible with a broad band centred around $2\theta \approx 34°$. It might have been nucleated directly in the undercooled melt, or it might have been formed because of re-heating of previously deposited coating material during subsequent torch passes.

Micro-Raman spectra acquired along the cross-section of the SrM-1 and OM-1 coatings consistently reveal the presence of the spinel phase (Fig. 6C), clearly recognisable by its characteristic main peak at about 675 cm^{-1}, with minor peaks at 310 cm^{-1} and 550 cm^{-1}.[42–44] The presence of the spinel spectrum across the whole coating suggests that this phase consists of small crystals, widespread throughout the sample, which can be easily justified by the very high nucleation rate and low grain growth rate imposed by the fast quenching of the molten lamellae. Accordingly, the Raman peaks of this spinel phase are quite weak and very broad, which indicates crystals are small and/or they contain numerous lattice defects, consistently with a very rapid solidification process. No other Raman peaks are identifiable: the secondary (glassy or perovskite-type) phase is either not generating any Raman signal, or its bands are too weak and are covered by the spectrum of the spinel phase.

The coatings deposited with no H_2 in the plasma gas mixture, by contrast, are significantly different. They indeed exhibit a bimodal microstructure (Figs. 3B, C and 4B, C), with dense regions entraining highly porous unmelted areas, where the original hexaferrite particles (either in the form of individual particles, as in type-A feedstock, or in the form of small crystalline grains obtained by reactive sintering, as in type-B feedstock) are retained. Dense regions clearly originate from fully melted or partly melted agglomerates, which solidify either onto the substrate (following impact quenching) or in flight (before impacting onto the substrate).

Fractured sections also highlight the presence of such bimodal microstructure. Specifically, in the coatings obtained from type-A feedstock (coating SrM-2 is shown in Fig. 7A), flattened lamellae, originating from the impact of fully molten agglomerates, coexist with highly porous unmelted regions where individual hexaferrite particles can easily be identified. Well-flattened lamellae exhibit a fine columnar structure (Fig. 7B) also described in the literature,[30,45] which witnesses to a high heterogeneous nucleation rate and a comparatively lower grain growth rate, confirming the previous assumptions on the very fast solidification process occurring upon impact quenching.

Although the OM-2 and OM-3 coatings obtained from type-B feedstock exhibit the same bimodal microstructure as the SrM-2 and SrM-3 ones, detailed views at higher magnification highlight a very important difference. Some of the original hexaferrite polygonal crystals can indeed still be recognised inside the dense regions originated by the solidification of molten material. A molten lamella entraining some unmelted crystals is shown in Fig. 8A, whereas Fig. 8B and C display unmelted polygonal crystals inside a dense region with dendritic microstructure.

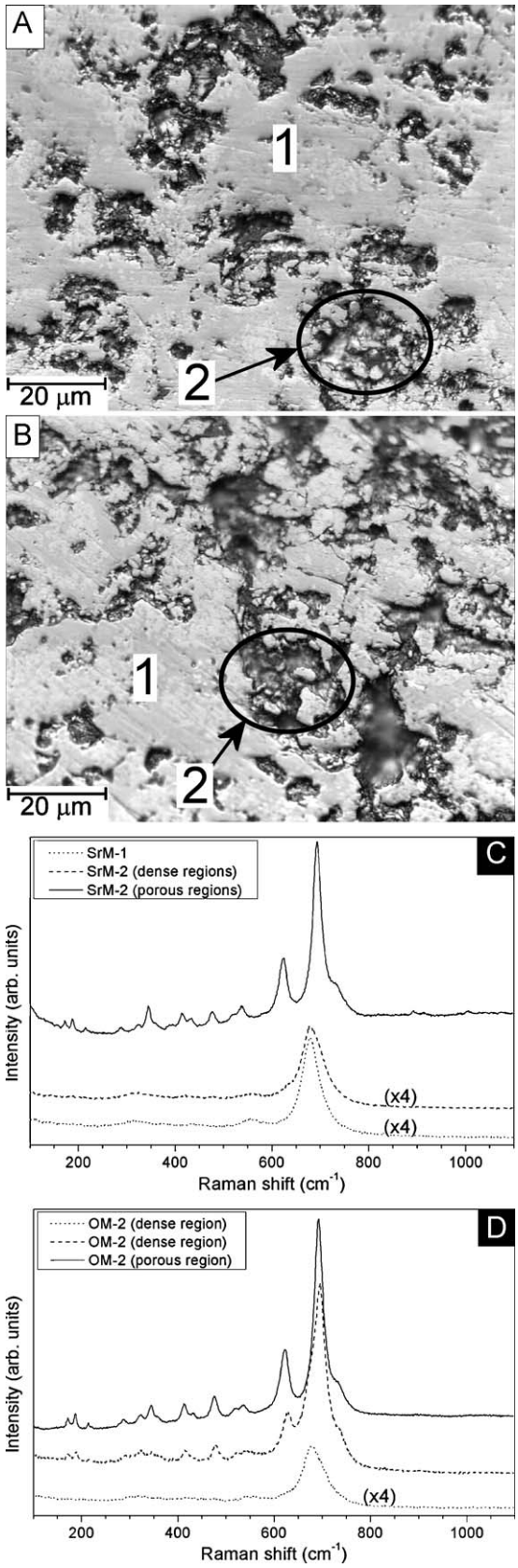

Fig. 6. Optical micrographs of the SrM-2 (A) and OM-2 (B) coatings (label 1 = dense regions, label 2 = porous regions) and Raman spectra acquired on the SrM-1 and 2 coatings (C) and on the OM-2 coating (D), respectively.

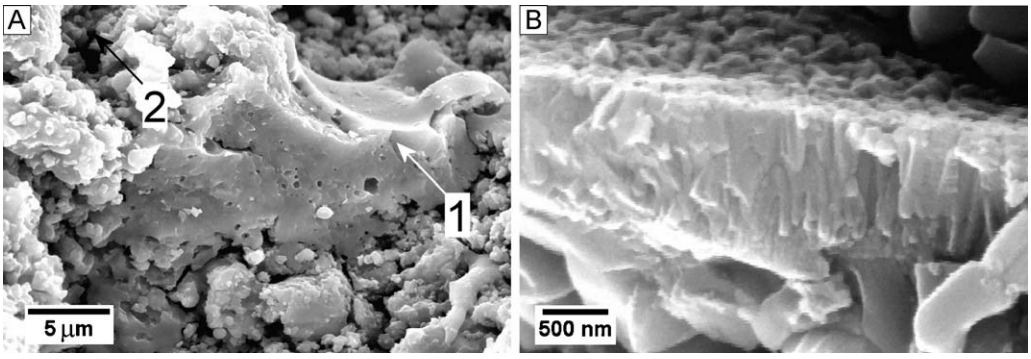

Fig. 7. SEM micrographs of the fractured section of coating SrM-2. (A) Overview (1 = flattened lamellae originating from molten agglomerates; 2 = unmelted regions) and (B) detail of fine columnar crystals inside a lamella.

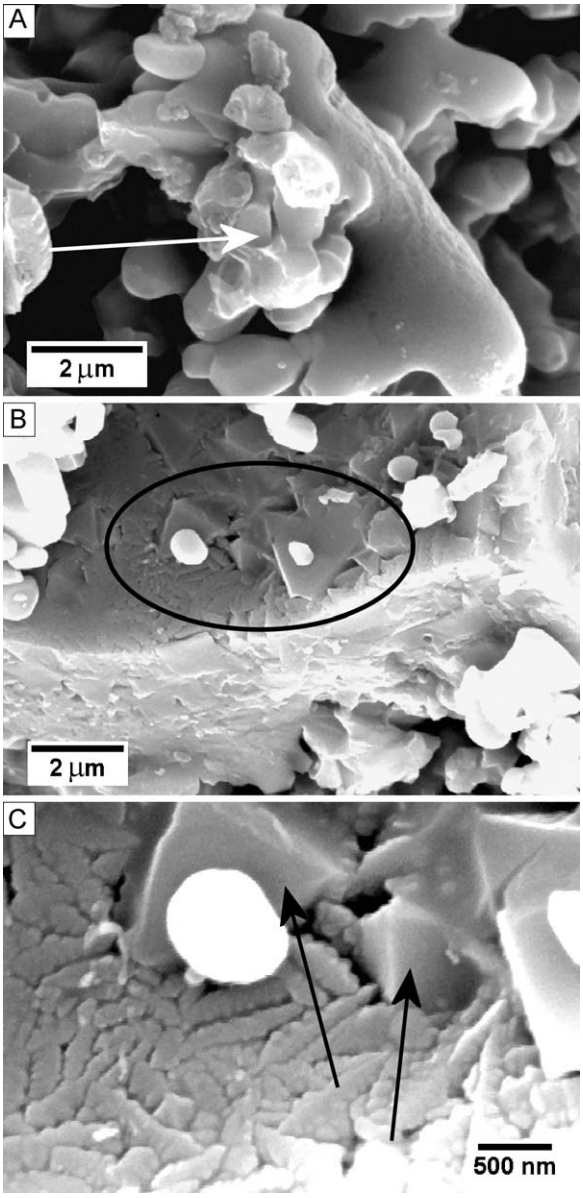

Fig. 8. SEM micrographs of the fractured section of coating OM-2. (A) Molten lamella entraining some unmelted polygonal hexaferrite crystals in its core; (B) dense region with dendritic microstructure, entraining some unmelted hexaferrite crystals; and (C) detail of the area circled in panel (B).

Dendrites consist most likely of magnetite, surrounded by the poorly crystalline (glassy or perovskite-type) matrix produced by the residual molten fraction.

The retention of unmelted hexaferrite crystals within the dense regions in coatings obtained from type-B feedstock has remarkable consequences on the phase distribution in those coatings. XRD patterns reveal the co-existence of spinel (magnetite) and of crystalline hexaferrite (Fig. 5A, B) both in the SrM-2 and SrM-3 coatings, obtained using type-A feedstock, and in the OM-2 and OM-3 coatings, obtained using type-B feedstock. Significant differences, however, exist between the distributions of these phases within the two distinct regions (dense ones and porous unmelted ones), which constitute the bimodal microstructure of these coatings. In the SrM-2 and SrM-3 coatings, crystalline hexaferrite was retained only in the porous unmelted regions. Accordingly, the only crystalline phase found in all of the dense regions of the SrM-2 and SrM-3 coatings (shown in Fig. 6A, label 1) is spinel (Raman spectrum in Fig. 6C), whereas the typical micro-Raman spectrum of the porous areas (one of them is shown in Fig. 6A, label 2), provided in Fig. 6C, matches with the one of Sr-hexaferrite given in.[46] By contrast, in the OM-2 and OM-3 coatings, crystalline hexaferrite exists both in the porous, fully unmelted regions (Fig. 6B, label 2) and in the dense regions (Fig. 6B, label 1). Specifically, in these latter, both the Raman spectrum of hexaferrite and that of spinel (magnetite) can be found at distinct locations (Fig. 6D). The spinel phase originated in the molten and resolidified portions of the dense regions, probably together with the poorly crystalline phase (not detectable in the Raman spectra, as mentioned previously), whereas crystalline hexaferrite is clearly contributed by the unmelted polygonal crystals entrained within such regions (as shown in Fig. 8).

Consequently, the diffraction peaks of the spinel phase are weaker (relative to the hexaferrite peaks) in the XRD patterns of the OM-2 and OM-3 coatings than in those of the SrM-2 and SrM-3 coatings, witnessing to higher hexaferrite retention when type-B feedstock is employed.

3.3. Magnetic properties of the APS coating layers

The amount and distribution of the Sr-hexaferrite phase in the two different categories of coatings have a direct effect on their

Table 2
Static magnetic properties of the as-deposited coatings.

Sample label	Feedstock type	M_{max} (emu/g)	Mr (emu/g)	Hc (Oe)
SrM-1	Type-A	57	13	620
SrM-2	Type-A	62	18	411
SrM-3	Type-A	63	21	678
OM-1	Type-B	61	13	249
OM-2	Type-B	57	21	757
OM-3	Type-B	60	25	1073
$SrFe_{12}O_{19}$[38,39]	–	55–75[a]		1000–6000
Magnetite[5]	–	92[a]		$\ll$1000

[a] Saturation magnetization.

static magnetic properties (Table 2), especially on their coercivity (Hc). It should preliminarily be reminded that Hc does not depend directly on the mass fraction of a particular magnetic phase and that Hc is an extrinsic property influenced by many factors, including crystallinity, microstructure, mechanical stress, etc. Nevertheless, the high Hc value (1073 Oe) of the OM-3 coating clearly suggests the existence of well-crystallised Sr-hexaferrite phase in this coating; indeed, Sr-hexaferrite intrinsically possesses much larger Hc than magnetite (Table 2). In contrast to this, the very low Hc value (249 Oe) of the OM-1 coating suggests that this coating consists (mostly) of magnetite.

It has to be noted that maximum magnetization (M_{max}) values listed in Table 2 are the magnetization values measured at the maximum applied magnetic field (13.5 kOe). As shown in Fig. 9 only the magnetization of the OM-1 sample saturated, while

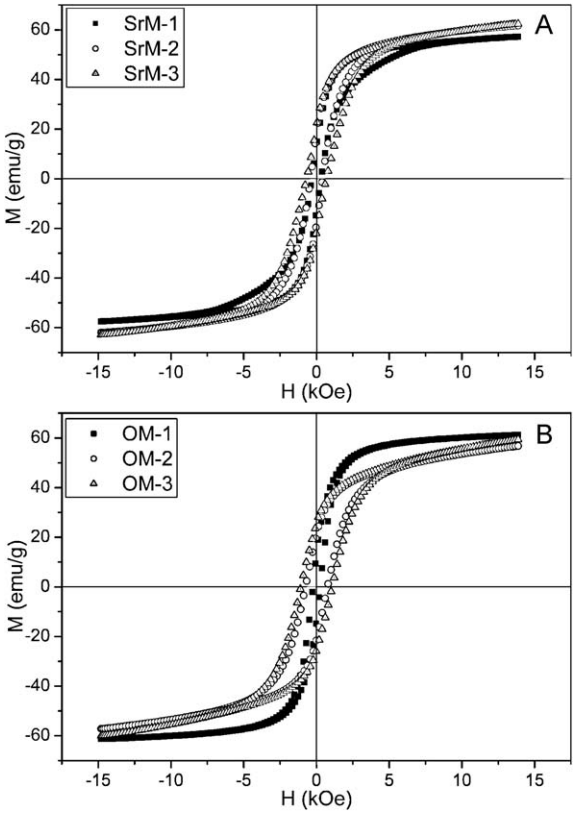

Fig. 9. Hysteresis curves of the SrM (A) and OM (B) coatings.

larger external field is required to saturate the other samples due to the high magnetocrystalline anisotropy of the Sr-hexaferrite (19 kOe). It can also be noted that the M_{max} values of the various coatings do not differ significantly. This can be explained by observing that these coatings are composed of two magnetic phases, Sr-hexaferrite and magnetite, and one non-magnetic phase (the poorly crystalline phase) in various proportions. As suggested by the XRD and Raman analyses (see Section 3.2 and Figs. 5 and 6), the fraction of the non-magnetic phase is inversely proportional to the fraction of the Sr-hexaferrite phase. The OM-coatings could be expected to possess lower M_{max} than the SrM-coatings because of their larger Sr-hexaferrite/magnetite phase ratio (magnetite indeed possesses larger intrinsic saturation magnetisation than Sr-hexaferrite, Table 2); however, this is compensated by the smaller fraction of the non-magnetic phase in the OM-coatings. Consequently, all of the coatings show similar M_{max}.

The OM-3 coating shows the best magnetic properties (Table 2), including the highest remanent magnetization (Mr). All of these properties are comparable to the values of Sr-hexaferrite, known from the pertinent literature.[47,48] The expected absorption characteristics of a Sr-hexaferrite layer were therefore calculated based on the complex permeability and permittivity behaviour of bulk Sr-hexaferrite. Such behaviour indicates ferromagnetic resonance at about 51–52 GHz (Fig. 10A), which confirms this material is actually promising for mm-wave applications, as expected (see Section 1). The calculations of the expected absorption of a pure Sr-hexaferrite layer predict a maximum attenuation of −16 dB at about 51 GHz when the coating is approximately 150–200 μm thick (Fig. 10B), which means that only 2.5% of the incident power is reflected back from the coated surface, i.e. 97.5% of the incident power is absorbed. This study has shown that $SrFe_{12}O_{19}$ coatings with such thickness can be obtained by APS. All these observations accordingly suggest that the APS technology is definitely suitable for the direct preparation of Sr-hexaferrite coatings, which are promising candidates for mm-wave absorbers.

3.4. Hypothesis on the in-flight behaviour of the two feedstock powders

The properties (phase composition and phase distribution, magnetic characteristics) of the coatings deposited using no H_2 in the plasma gas mixture seem to be controlled by the different behaviour of the two kinds of feedstock powders during the spraying process. More specifically, the results in Section 3.2 suggest that, when reactively sintered agglomerates (type-B feedstock) melt, they are generally able to retain a certain amount of unmelted hexaferrite crystals. By contrast, when the spray-dried agglomerates of hexaferrite particles (type-A feedstock) melt, they seem not to leave any residual unmelted fraction. Consequently, when this latter kind of feedstock is employed, the only way to retain some crystalline hexaferrite in the coatings is to embed a certain amount of unmelted agglomerates. When type-B feedstock is employed, by contrast, crystalline hexaferrite is contributed both by unmelted agglomerates and by

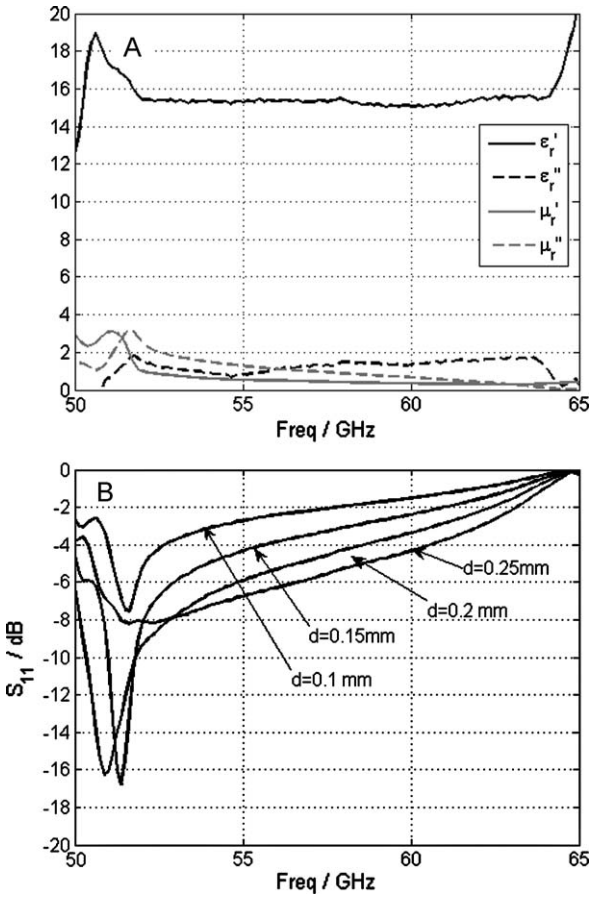

Fig. 10. Complex permeability and permittivity behaviour of bulk sintered $SrFe_{12}O_{19}$ (A) and calculated absorption by a metal plate coated with pure $SrFe_{12}O_{19}$ layers of various thicknesses (B).

partly melted ones; therefore, its overall amount in the resulting coatings is larger, which has obvious favourable effects on the magnetic properties, as discussed in Section 3.3.

The following hypothesis on the in-flight behaviour of the two kinds of feedstock can be put forward in order to explain this difference. Type-B agglomerates possess some internal cohesion, on account of the reactive sintering process, so that most of them do not disrupt when they are injected into the plasma jet. Depending on their size and trajectory, some experience poor heating and do not melt, whereas others are better heated and develop a molten layer on their outer portion.[49,50] Because of their high porosity, however, these agglomerates possess low thermal conductivity; therefore, even when the heat input is sufficient to melt their outer part, their inner core does not melt and retains the crystalline Sr-hexaferrite structure. The molten material from the outer shell can infiltrate the pores of the unmelted inner core and densify the entire agglomerate. When such partly melted system solidifies, either upon impact with the substrate or in-flight (before impact), it produces a dense coating area where unmelted hexaferrite crystals are entrained in a matrix consisting of spinel (magnetite) + Sr-rich residual phase, generated by the solidification of the liquid fraction (as seen in Fig. 8).

Type-A agglomerates, by contrast, were spray-dried with no further consolidation treatment; therefore, their cohesive strength is much poorer. It can be speculated that some of the agglomerates which do not enter the plasma core do not disrupt and remain entirely unmelted. Most of those which enter the plasma core are probably broken apart (break-up of spray-dried agglomerates during thermal spraying was clearly suggested in Ref. [51]). Specifically, they can either be divided into few smaller agglomerates (secondary agglomerates) or be completely disrupted into micrometric individual particles and/or very small aggregates of few individual particles. In this latter case, the material is probably lost without deposition: very small aggregates or individual micrometric particles have extremely low mechanical and thermal inertia, so that they resolidify completely and slow down significantly before reaching the substrate.[52–54] In the first case, by contrast, the secondary agglomerates melt completely and eventually give rise to dense coating regions with no residual crystalline hexaferrite. Accordingly, fracture surface views highlight that the diameter of most of the flattened lamellae is <20 μm, which means that they originate from molten droplets of less than 6–7 μm in diameter, if a flattening ratio of 3 is conservatively assumed (the size of the droplet may even be smaller if higher flattening ratios are actually attained: literature values are frequently ≥4, as shown e.g. in Refs. [30,55]). Type-A feedstock, however, exhibits d_{10} = 18 μm (Section 3.1). So, most of the lamellae are not produced by the original agglomerates, but by smaller secondary agglomerates.

It can be concluded that the reactively sintered feedstock (type-B) is more promising for further optimisation of the layers. It is indeed clear that the present coatings still need improvements, as they are probably too porous and weak, and sometimes not perfectly homogeneous. With type-A feedstock, however, a high amount of crystalline hexaferrite in the coatings can only be achieved at the expense of the final density of the coating itself, since the only way to attain such goal is to increase the amount of unmelted agglomerates during spraying. With type-B feedstock, by contrast, the phenomenon of partial melting of the reactively sintered agglomerates, with the unmelted core being infiltrated and densified by the molten outer shell, can be exploited in order to obtain layers with adequate hexaferrite content while preserving acceptable coating density. Presumably, further work on the processing of type-B feedstock shall therefore lead to denser and more homogeneous coatings, yet sufficiently rich in crystalline hexaferrite and suitable for industrial applications.

4. Conclusions

Two different kinds of $SrFe_{12}O_{19}$ hexagonal ferrite (hexaferrite) powders, suitable as feedstock for the atmospheric plasma spraying (APS) process, were manufactured. One consisted of spray-dried spherical agglomerates of micrometric hexaferrite particles, synthesised by solid-state reaction between suitable reagents and subsequent attrition milling. The other consisted of spray-dried agglomerates of reagent particles ($SrCO_3$ and Fe_2O_3), which were reactively sintered in order to achieve consolidation and complete conversion to crystalline stoichiometric hexaferrite. Both kinds of feedstock powders were processed by APS, aiming to deposit coatings which retain sufficient amounts of crystalline hexaferrite. The high magnetic losses of crys-

talline $SrFe_{12}O_{19}$ at about 50 GHz indicate that such coatings are promising candidates for electromagnetic absorbers in the mm-wave range.

The following conclusions can be drawn from the experimental results:

- Melting of the feedstock powder during the spraying process irreparably compromises the crystalline hexaferrite structure. Melt solidification indeed develops spinel (magnetite) and a secondary phase with poor crystallinity.
- Crystalline hexaferrite-rich coatings must therefore be obtained by embedding an adequate amount of unmelted material inside them, which requires proper adjustments of the process parameters.
- Hexaferrite-rich APS layers always exhibit bi-modal microstructure, consisting of porous regions (generated by unmelted agglomerates) entrained in a dense matrix, produced by the solidification of partly melted or fully melted agglomerates.
- In all cases, the porous unmelted regions consist of unaltered crystalline hexaferrite.
- The phase distribution within the dense regions depends on the type of feedstock powder. When reactively sintered feedstock is employed, the dense regions contain an intimate mixture of spinel, secondary poorly crystalline phase and residual unmelted crystalline hexaferrite. By contrast, spray-dried agglomerates of pre-reacted particles yield dense regions consisting of spinel and secondary phases only, with no residual unmelted hexaferrite.
- The reactively sintered feedstock is therefore more promising for further optimisation of the coatings: sufficiently high amounts of unmelted hexaferrite can indeed be embedded in the layers without impairing the coating density too much.

Acknowledgements

This work was done in the frame of the EU6, MATERA ERA-NET, 4302-31/2006/26, ABSOFILM project. The authors would like to thank the financial support of the Ministry for Higher Education, Science and Technology of the Republic of Slovenia, of the Ministry of Innovation, Science, Research and Technology of the State of North Rhine-Westphalia, Germany, and of Tekes, Finnish Funding Agency of Technology and Innovation.

References

1. Koledintseva MY, Kitaytsev AA, Shinkov AA. Microwave filtering of unwanted oscillations on base of hexagonal ferrite composite thick films. In: *Proceedings of the IEEE international symposium on electromagnetic compatibility, vol. 1*. 1998. p. 578–82.
2. Lebed BM, Voronkov VD. State of the art millimeter and sub-millimeter wave ferrite components and devices. In: *Proceedings of the 26th European Microwave Conference, vol. 2*. 1996. p. 816–22.
3. Shin JY, Oh JH. The microwave absorbing phenomena of ferrite microwave absorbers. *IEEE Trans Magn* 1993;**29**:3437–9.
4. Amano M, Kotsuka Y. A method of effective use of ferrite for microwave absorber. *IEEE Trans Microwave Theory Tech* 2003;**51**:238–45.
5. Smit J, Wijn HPJ. *Ferrites, Chapter IX*. Eidenhoven: Philips' Technical Library; 1959.
6. Brard C, Taffary T, Autissier D, Jorion F. Influence on Fe^{2+} on microwave behaviour of $M(Co, Ti)_{1.2}$ type hexaferrite. *J Phys IV France* 1998;**8**. Pr2-401–4.
7. Vincent H, Sugg B, Lefez V, Bochu B, Boursier D, Chaudouet P. Crystal growth, X-ray and magnetic studies of planar anisotropy M-hexaferrites $BaFe_{12-2x}Ir_xMe_xO_{19}$ (Me = Zn, Co). *J Magn Magn Mater* 1991;**101**:170–2.
8. Zhou XZ, Morrish AH, Yang Z, Zeng H-X. Co–Sn substituted barium ferrite particles. *J Appl Phys* 1994;**75**:5556–8.
9. Du Pre FK, De Bitetto DJ, Brockman FG. Magnetic materials for use at high microwave frequencies (50–90 kMc/sec). *J Appl Phys* 1958;**29**:1127–8.
10. Sugimoto S, Haga K, Kagotani T, Inomata K. Microwave absorption properties of Ba-M type ferrite produced by a modified coprecipitation method. *J Magn Magn Mater* 2005;**290/291**:1188–91.
11. Li ZW, Chen L, Ong CK. Studies of static and high-frequency magnetic properties for M-type ferrite $BaFe_{12-2x}Co_xZr_xO_{19}$. *J Appl Phys* 2002;**92**:3902–7.
12. Heimann RB. Applications of plasma-sprayed ceramic coatings. *Key Eng Mater* 1996;**122–124**:399–442.
13. Herman H, Sampath S, McCune R. Thermal spray: current status and future trends. *MRS Bull* 2000;**25**(7):17–25.
14. Bartuli C, Cipri F, Valente T. Thermal spraying and the fabrication of coatings with tailored electro-magnetic properties. *Inorg Chim Acta* 2008;**361**:4077–88.
15. Ge S, Ma X, Zhang T, Wu M, Zhang H, Zhang YD, et al. Structural and magnetic properties of nanostructured $Ni_{0.5}Zn_{0.5}Fe_2O_4$ films fabricated by thermal spray. *J Appl Phys* 2003;**93**:7498–500.
16. Yan QY, Gambino RJ, Sampath S, Huang Q. Neutron diffraction and ferromagnetic resonance studies on plasma-sprayed MnZn ferrite films. *J Appl Phys* 2005;**97**:0033902.
17. Yan Q, Gambino RJ, Sampath S, Lewis LH, Li L, Baumberger E, et al. Effects of zinc loss on the magnetic properties of plasma-sprayed MnZn ferrites. *Acta Mater* 2004;**52**:3347–53.
18. McCartney DG, Zhang D, Yellup JY, Brühl M, Bobzin K, Richardt K, et al. Novel NiZn-ferrite powders and coatings for electromagnetic applications. In: Marple BR, Hyland MM, Lau Y-C, Li C-J, Lima RS, Montavon G, editors. *Expanding thermal spray performance to new markets and applications—proceedings of the 2009 international thermal spray conference*. Materials Park, OH, USA: ASM International; 2009. p. 818–23.
19. Vidal EE, Taylor PR. Thermal plasma synthesis of $BaFe_{12}O_{19}$ (BaM) films. *Plasma Chem Plasma Process* 2003;**23**:609–26.
20. Lisjak D, Bobzin K, Richardt K, Bégard M, Bolelli G, Lusvarghi L, et al. Preparation of barium hexaferrite coatings using atmospheric plasma spraying. *J Eur Ceram Soc* 2009;**29**:2333–41.
21. Lisjak D, Makovec D, Gyergyek S, Hujanen A, Lintunen P, Varis T, et al. The preparation of barium hexaferrite coatings using HVOF. *J Am Ceram Soc* 2009;**92**:818–24.
22. Bégard M, Bobzin K, Bolelli G, Hujanen A, Lintunen P, Lisjak D, et al. Thermal spraying of Co,Ti-substituted Ba-hexaferrite coatings for electromagnetic wave absorption applications. *Surf Coat Technol* 2009;**203**:3312–9.
23. Bobzin K, Schlaefer T, Bégard M, Bruehl M, Bolelli G, Lusvarghi L, et al. Development of Ba-hexaferrite coatings for electromagnetic wave absorption applications. *Surf Coat Technol* 2010;**205**:1015–20.
24. Hewlett-Packard Product Note 8510-3; 1985.
25. Arcondéguy A, Grimaud A, Denoirjean A, Gasgnier G, Huguet C, Pateyron B, et al. Flame-sprayed glaze coatings: effects of operating parameters and feedstock characteristics onto coating structures. *J Therm Spray Technol* 2007;**16**:978–90.
26. Bolelli G, Rauch J, Cannillo V, Killinger A, Lusvarghi L, Gadow R. Investigation of high-velocity suspension flame sprayed (HVSFS) glass coatings. *Mater Lett* 2008;**62**:2772–5.
27. Guo HB, Vaßen R, Stöver D. Atmospheric plasma sprayed thick thermal barrier coatings with high segmentation crack density. *Surf Coat Technol* 2004;**186**:353–63.
28. Matejicek J, Sampath S, Gilmore D, Neiser R. In situ measurement of residual stresses and elastic moduli in thermal sprayed coatings: Part 2: Processing effects on properties of Mo coatings. *Acta Mater* 2003;**51**:873–85.

29. Van Hook HJ. Thermal stability of barium ferrite ($BaFe_{12}O_{19}$). *J Am Ceram Soc* 1964;**47**(11):579–81.
30. Fauchais P, Fukumoto M, Vardelle A, Vardelle M. Knowledge concerning splat formation: an invited review. *J Therm Spray Technol* 2004;**13**:337–60.
31. Wang XY, Zhang H, Zheng LL, Sampath S. An integrated model for interaction between melt flow and non-equilibrium solidification in thermal spraying. *Int J Heat Mass Transfer* 2002;**45**:2289–301.
32. Langhof N, Seifert D, Göbbels M, Töpfer J. Reinvestigation of the Fe-rich part of the pseudo-binary system SrO–Fe_2O_3. *J Solid State Chem* 2009;**182**:2409–16.
33. Li L, Kharas B, Zhang H, Sampath S. Suppression of crystallization during high velocity impact quenching of alumina droplets: observations and characterization. *Mater Sci Eng A* 2007;**456**:35–42.
34. Dent AH, Patel A, Gutleber J, Tormey E, Sampath S, Herman H. High velocity oxy-fuel and plasma deposition of $BaTiO_3$ and (Ba,Sr)TiO_3. *Mater Sci Eng B* 2001;**87**:23–30.
35. Ctibor P, Ageorges H, Sedlacek J, Ctvrtlik R. Structure and properties of plasma sprayed $BaTiO_3$ coatings. *Ceram Int* 2010;**36**:2155–62.
36. Kajima A, Kaneda T, Ito H, Fujii T, Okamoto I, Kimura T, et al. Ferromagnetic amorphouslike oxide films of the Fe_2O_3–Bi_2O_3–$PbTiO_3$ system prepared by rf-reactive sputtering. *J Appl Phys* 1991;**69**:3663–9.
37. Kim S-G, Wang W-N, Iwaki T, Yabuki A, Okuyama K. Low-temperature crystallization of barium ferrite nanoparticles by a sodium citrate-aided synthetic process. *J Phys Chem C* 2007;**111**:10175–80.
38. Zhang HY, Gu BX, Zhai HR, Miao YZ, Lu M. New phenomena in FMR and EPR studies of amorphous oxide films and their crystallization. *J Magn Magn Mater* 1995;**139**:115–8.
39. Wu A, Cheng G, Shen H, Xu J, Chu Y, Ge Z. Preparation of $ReFeO_3$ nanocrystalline powders by auto-combustion of citric acid gel. *Asia-Pac J Chem Eng* 2009;**4**:518–21.
40. Park JH, Kim KY, Park SD. Oxygen permeation and stability of $La_{0.6}Sr_{0.4}Ti_xFe_{1-x}O_{3-\delta}$ ($x = 0.2$ and 0.3) membrane. *Desalination* 2009;**245**:559–69.
41. Kumar Singh S, Kumar J. On the structural, magnetic and oxygen desorption response of $Ba_xSr_{1-x}Fe_{0.8}Co_{0.2}O_{3-\delta}$ ($x = 0$, 0.5 and 1) oxide. *J Alloys Compd* 2009;**481**:455–61.
42. de Faria DLA, Venâncio Silva S, de Oliveira MT. Raman microspectroscopy of some iron oxides and oxyhydroxides. *J Raman Spectrosc* 1997;**28**:873–8.
43. Maslar JE, Hurst WS, Bowers WJ, Hendricks JH, Aquino MI. In situ raman spectroscopic investigation of aqueous iron corrosion at elevated temperatures and pressures. *J Electrochem Soc* 2000;**147**:2532–42.
44. Da Cunha Belo M, Walls M, Hakiki NE, Corset J, Picquenard E, Sagon G, et al. Composition, structure and properties of the oxide films formed on the stainless steel 316L in a primary type PWR environment. *Corros Sci* 1998;**40**:447–63.
45. Bianchi L, Denoirjean A, Blein F, Fauchais P. Microstructural investigation of plasma-sprayed ceramic splats. *Thin Solid Films* 1997;**299**:125–35.
46. Morel A, Le Breton JM, Kreisel J, Wiesinger G, Kools F, Tenaud P. Sublattice occupation in $Sr_{1-x}La_xFe_{12-x}Co_xO_{19}$ hexagonal ferrite analyzed by Mössbauer spectrometry and Raman spectroscopy. *J Magn Magn Mater* 2002;**242/245**:1405–7.
47. Haneda K, Miyakawa C, Goto K. Preparation of small particles of $SrFe_{12}O_{19}$ with high coercitivity by hydrolysis of metal-organic complexes. *IEEE Trans Magn* 1987;**23**:3134–6.
48. Fang J, Wang J, Gan LM, Ng SC, Ding J, Liu X. Fine strontium ferrite powders from an ethanol-based microemulsion. *J Am Ceram Soc* 2000;**83**:1049–55.
49. Williamson RL, Fincke JR, Chang CH. A computational examination of the sources of statistical variance in particle parameters during thermal plasma spraying. *Plasma Chem Plasma Process* 2000;**20**:299–324.
50. Ang CB, Ng HW, Yu SCM, Lam YC. A proposed process control chart for DC plasma spraying process. *Plasma Chem Plasma Process* 2000;**20**:325–42.
51. Fogarassy P, Gerday D, Lodini A. Agglomerated nanostructured particles disintegration during the plasma thermal spraying process. *Mech Res Commun* 2005;**32**:221–39.
52. Fauchais P. Understanding plasma spraying. *J Phys D Appl Phys* 2004;**37**:R86–108.
53. Vardelle M, Vardelle A, Fauchais P, Li K-I, Dussoubs B, Themelis NJ. Controlling particle injection in plasma spraying. *J Therm Spray Technol* 2001;**10**:267–84.
54. Dongmo E, Wenzelburger M, Gadow R. Analysis and optimization of the HVOF process by combined experimental and numerical approaches. *Surf Coat Technol* 2008;**202**:4470–8.
55. Li C-J, Liao H-N, Gougeon P, Montavon G, Coddet C. Experimental determination of the relationship between flattening degree and Reynolds number for spray molten droplets. *Surf Coat Technol* 2005;**191**:375–83.